# Study of the role of surface oxide on electrodeposited single crystal Bi Nanowires

M. Plaza[1], M. Abuín[1], S. Sangiao[2,3], N. Marcano[2], J. de la Venta[1], M.A. García[4], J.M. de Teresa[2], L. Morellón[2,3], M.C. Sánchez[1] and L. Pérez[1,*]

[1] Dept. Física de Materiales, Universidad Complutense de Madrid, Madrid 28040 Spain

[2] Instituto de Ciencia de Materiales de Aragón, Universidad de Zaragoza-CSIC & Departamento de Física de la Materia Condensada, Universidad de Zaragoza, Zaragoza 50009, Spain

[3] Instituto de Nanociencia de Aragón, Universidad de Zaragoza, Zaragoza, 50009, Spain

[4] Insituto de Cerámica y Vidrio, CSIC

## INTRODUCTION

Bismuth is a semi-metal with unique electronic properties, which makes it a very interesting scenario to study size-dependant magnetotransport properties in micro and nanostructures. In particular, the mean free path ($l_f$) and the wavelength of electrons at the Fermi level ($\lambda_F$) are extremely large compared to most metals [1,2]. Due to these singular electronic properties, large magnetoresistance and a strong dependence of magnetotransport on the diameter ($d$) have been observed in bismuth nanowires (NWs) due to finite size effects [3,4] The observation of quantum size effect phenomena (QSE) in the magnetotransport is also expected because the density of states oscillates as a function of the diameter ($d$) for NWs with $d$ close to $\lambda_F$ [5]. Oscillations of resistivity due to QSE have been already reported in single Bi nanowires [6,7]. Some other size-effects have been also recently reported like the possible existence of surface states [8,9], signatures of weak antilocalization in the magnetotransport [10], superconductivity [11] or diameter-dependence of thermopower and magnetothermopower effects [12]. For the observation of all these phenomena and some others not measured yet - oscillations in magnetotransport or Hall resistivity - it is necessary to synthesize and manipulate individual MW with $d\sim\lambda_F$ and large grain size. Otherwise scattering processes mainly occur in grain boundaries, making impossible the observation of QSE.

In addition, the surface of Bi NWs is normally oxidized [13,14], which on one hand limits the technology that can be used for making ohmic contacts needed for transport measurements [7,10,15] and, on the other hand reduce the effective diameter of the nanowire for the transport measurements because only the inner part of each NW is conductive Bi. Therefore, a detailed

characterization of the oxide layer which covers the Bi NW is needed in order to correlate electronic properties and morphology. Among other techniques like pressure injection [16] or stress-induced methods [17], electrochemical deposition (ECD) using a nanoporous polycarbonate membranes (PCM) or anodized aluminum oxide as templates has been shown as a suitable technique for the synthesis of strongly textured Bi nanowires [18-20]. In this work, we present a comprehensive characterization of morphological, structural and electronic properties of Bi single NWs. We specially focused our work in the study of the native oxide which surrounds the as-deposited NWs hindering its use in spintronics.

## RESULTS AND DISCUSSION

### Electrodeposition of Bi NWs

NWs were synthesized by electrochemical deposition using polycarbonate membranes (PCM) with one side metalized with Au as working electrodes. The used PCMs have pore diameter ranging from 10 to 100nm. Au is commonly used as working electrode for Bi electrodeposition because Au surfaces do not requires chemical pre-treatment and present an Under Potential Deposition (UPD) in Bi(III) [21-25], which ensures a good nucleation of the NWs. This is essential in order to obtain high-quality crystalline structure in the NWs. Figure 1.a shows a typical current versus time transient measured during the growth of Bi NWs in a PCM of 30nm in diameter at $U_{dep}$=-75mV (hereafter, the values for growth potential ($U_{dep}$) are referred to the Ag/AgCl reference electrode). The transients present the expected line shape for electrodeposited NWs [26]. Three different regions can be distinguished in these curves, corresponding to three different growth regimes. Firstly, there is a rapid drop of the current due to nucleation of bismuth onto the Au layer (fig. 1.a.i). After the nucleation process, there is a steady regime due to the constant growth rate of bismuth while the channels are being filled, since the active surface is constant (fig. 1.a.ii). Finally, when the channels are completely filled, bismuth began to grow as thin films over the surface or the PCM, connecting the different pores. In this case, the active surface of the working electrode drastically increases producing an abrupt increase of the current for constant potential (fig. 1.a.iii). The growth is always stopped in the second regime, ensuring the formation of bismuth NWs.

In order to explore the influence of $U_{dep}$ on the ECD process, morphology and crystalline structure of the NWs, a series of NWs were grown varying $U_{dep}$ in 100nm pore size PCM. In a previous work [27], we showed that Bi films deposited at $U_{dep}$ below -100mV presented needle-like growth which impoverished the transport properties, On the other hand, Bi films obtained at $U_{dep}$ above -25mV are formed by poorly bonded grains. Therefore, we varied growth potential between these

values. All NWs were cylinder in shape and some of them preserved the Au seed at the beginning of the wire (fig. 1.b). Although the Au seed has basically the same diameter than the pore diameter of the PCM template, Bi NWs are clearly wider. We suggest that this effect, which can be observed in the first nanometers of the total length of the NWs, may be due to strain produced during the nucleation process. This effect is larger for those NWs grown at lower $U_{dep}$, which supports this explanation. We did not find any significant difference in the morphology of the NWs with the growth potential. However, we found notable differences in the NWs density in the templates as a function of $U_{dep}$. At higher deposition potentials (-25mV and -50mV), the density of Bi NWs was low and strongly inhomogeneous. This effect is due to the fact that at higher $U_{dep}$ (small overpotentials) the nucleation process is progressive [28]. In case of thin films, progressive nucleation generates a high roughness and a broad grain/island size distribution, but, in case of NWs, it causes the mentioned inhomogeneous nucleation in the template. On the other hand, as we indicated before, NWs deposited at very low potential (-100mV) present high strain during the nucleation and that may cause the presence of a high defects accumulation. Taking this into account, next experiments will be carried out setting $U_{dep}$=-75mV.

Once we determined the suitable $U_{dep}$, we carried out experiments varying the pore size of the PCMs. NWs resulted shorter than the PCM nominal thickness (about 6µm [29]), most likely due to the fact that Bi is very fragile and the NWs broke during their manipulation. NWs growth in PCM of 10nm and 30nm in pore size (fig. 1.c and 1.d) presented a diameter varying among 50nm to 90nm and very homogeneous along the wire. However, in case of 10nm in pore size, the diameter distribution was much broader. The NWs grown in PCMs of pore diameter of 50nm and 100nm (not shown here) were much wider than the $\lambda_F$ (~50nm) and their diameter varies about 85% along the wire.


**Crystalline Structure. Growth direction**

Figure 2.a shows the XRD patterns for NWs deposited at -75mV in PCMs from 10nm to 100nm of pore size. The as-measured patters showed an amorphous halo (15º<2θ<40º) due to the contribution of the amorphous holder and/or the PCMs residues. We have corrected it using X'Pert HighScore software [30] for a better observation of the Bi reflections. All patterns show reflections that can be indexed to the rhombohedral R-3m (166) structure. The presence of several peaks is due to the randomly distribution of the wires onto the surface of the holder when the PCM is dissolved. The differences among the patterns are practically negligible indicating that the texture of the NWs is not affected by the pore size. We have also carried out an exhaustive study of several nanowires grown at -75mV in different zones by HRTEM and SAED to determine

the growth direction. NWs grow preferentially along the (012) direction as can be seen in figures 2.b and 2.c, where the red arrows point to the (012) direction whereas the yellow ones point to the growth direction (parallel to the surface of the NW). It can be seen that growth directions are slightly deviated from (012). We think that these deviations are due to the difficulty in determining accurately the growth direction because of the surface roughness of the NWs. The HRTEM study also revealed that all NWs are single crystalline, which is also confirmed by the spotty SAED patterns (fig. 2.d). No extensive defects have been observed in the HRTEM images. However, low dimensional defects (i and ii in figure 2.c) have been found in some of them. This defects may be the cause of the small deviation among the growth and the (012) directions reported previously. In any case, these kinds of defects do not affect drastically the electronic properties of the NWs which are our main concern [10].

A carefully observation of the HRTEM images revealed a presence of an amorphous shell surrounding the Bi NWs (fig. 2.e). The presence of this oxide also affected the SAED patterns (fig. 2.d), where a halo is visible. The intensity of this halo is higher in case of narrower NWs than in the wider ones denoting that is related to the surface-to-volume ratio. EDX measurements confirm the presence of a low content of oxygen in the shell, about 15-20%. The thickness of the oxidized was between 5nm and 10nm.

**Oxidized layer**

XANES measurements allowed us to characterize the short range ordering of the Bi atoms in the NWs because of its atomic selectivity even in disordered compounds. We performed XANES experiments of the NWs at $L_3$ edge to characterize the oxidation state of the Bi atoms in the NWs. To compare, we also measured the XANES spectra of Bi and $Bi_2O_3$ in powder form as references. The Bi powder was milled immediately before to the XANES scans to prevent the oxidation. Figures 3.a and 3.b show the XANES spectra and their corresponding derivative spectra of Bi NWs, Bi powder and BiO powders. The line shape for Bi and BiO spectra are in good agreement with the reported before [31,32]. The differences among the XANES spectra for unoxidized NWs were negligible revealing that the oxidation state is the same irrespective of the NW diameter. Moreover, their line shape is closer to the Bi spectrum.

The absorption edge is defined as the maximum in the derivative XANES spectra. Then, the comparison between the references and NWs spectra provides information about the shift of the absorption edge. Since Figure 3.b, it can be noticed that the derivative spectrum of Bi powder has

three well differentiated peaks (labeled A1, A2 and A3). These peaks are clearly presented also in spectra of the unoxidized NWs. The most intense BiO peak (labeled B) appears at 4eV shifted toward higher energies with respect to the Bi most intense one. The most intense peak of NWs spectra presents a shoulder at the position of B peak due to the contribution of the BiO of the shell. We have estimated the amount of BiO in the NWs from the XANES spectrum of Bi ($\beta_{Bi}$) and BiO ($\beta_{Ox}$) for the different NWs. To carry out this estimation, we have defined $p$ as the ratio of Bi atoms with a similar neighborhood that the Bi atoms in the BiO structure. So $p$ is approximately the value of the amount of BiO in the NWs. In that sense, we calculated the NWs spectrum ($\beta$) using the following expression:

$$\beta = (1-p)\,\beta_{Bi} + p\,\beta_{Ox} \tag{1}$$

In figure 3.a, we show the calculated spectra from the previous equation (dotted lines). We found the best agreement between the experimental measurements at the calculated spectra for p=23.0%, 22.0% and 21.5% for NWs grown in PCMs of 10nm, 30nm and 50nm in diameter respectively. These results indicate that the concentration of BiO in the NWs is not related to the size of the NWs, because the amount of bismuth oxide is practically the same (~22%). We want to remark that this is an approximation which provides the correct tendency but not an exact value because we are comparing bulk reference samples with NWs and non-saturated surface bonds can modify XANES spectra. From these estimations, we can calculate the thickness of the bismuth oxide shell as a function of the diameter in order to compare with the experimental results obtained in the HRTEM experiments (fig 2.e). We define $r$ as the radius of the Bi core, $t$ as the thickness of the oxidized shell and $L$ as the total length of the NW. Then, the volume of the Bi core NW ($V_{Bi}$) and oxidized shell ($V_{Ox}$) are $V_{Bi} = L\pi\,r^2$ and $V_{Ox} = L\pi\,[(r+t)^2 - r^2]$. Using these equations, we calculated the ratio between the oxidized bismuth and Bi ($\alpha$) as:

$$\alpha = V_{Ox}\,/\,V_{Bi} = (t^2 + 2tr)\,/\,2r^2 \tag{2}$$

From this expression we obtain $t = r[(1+\alpha)^{\frac{1}{2}} - 1]$. Replacing the estimated value of $\alpha$ from the XANES fitted spectrum, we found that the thickness of the oxidized shell is $t \approx 0.1r$. This value is in good agreement with the one found by HRTEM. Therefore, we can conclude that the oxygen is basically located at the shell, whereas the inner part of the NWs is formed by pure Bi.

We also measured Bi NWs (50nm in diameter) completely oxidized. To achieve them, we preserved the Bi NWs during 10 days unprotected against the atmospheric oxygen. The XANES

spectrum of these NWs was equal to the BiO pattern and its derivative spectrum was also similar. It presented the characteristic peak 4eV above the edge of Bi. This oxidation process is also confirmed by XRD measurements. XRD patterns of oxidized NWs are shown in figure 3.c. The presence of a new peak (dashed line) close to the Bi(012) (solid line) is evident and its intensity is strongly dependent on the diameter of the pore. We attribute this peak to the existence of crystalline $Bi_2O_3$ in the NWs. This reflection can be indexed to [120] $Bi_2O_3$ monoclinic P21/C (14) and/or [310] $Bi_2O_3$ cubic I23 (197) structures.

**Thermal evolution of resistivity**

A four-probe on an individual Bi NW nanodevice is crucial in order to explore fundamental transport properties. In the present case Focused-ion beam techniques have been used to fabricate the four Tungsten-based nanocontacts [10] on individual 100 nm-diameter nanowires showed in Fig. 4 (c). From I-V measurements, the contacts were observed to the Ohmic at both temperatures of 5 and 300 K, corresponding to resistivities $\rho$ of 1.83 x $10^{-3}$ $\Omega$ cm and 6 x $10^{-4}$ $\Omega$ cm , respectively (see Fig. 4 (b). This fact indicates that the achieved contacts allow reliable transport measurements in the studied temperature range, and thus, the observed Bi oxide shell has been either partly removed during the contact fabrication using the ion-beam or, if still present, is not thick enough to disrupt the electrical transport. The temperature dependence of resistance R(T) for the individual 100-nm-diameter Bi NW in the temperature range of 5-300K is shown in Fig.4 (a). The resistance increases with decreasing temperature, i.e., the temperature coefficient of resistance (TCR) is negative.  In bulk Bi, the TCR is positive, while negative TCR is usually observed in Bi thin films. This is because the main contributions to the TCR in Bi are due to carrier concentration and mobility, which have opposite temperature dependence. With increasing temperature, the carrier concentration increases, whereas the carrier mobility decreases, leading to a respectively a negative and a positive TCR. Thus, the competition between these two opposing contributions determines the TCR sign of a Bi sample. When carrier mobility is suppressed by structural imperfections or finite-size effects, the carrier concentration dominates the TCR.  In the present case of 100 nm-diameter NW, because of the smaller wire diameter in comparison with the mean free path, the TCR is negative.

## METHODS

### Electrolyte preparation

The electrolyte was an aqueous 10 vol.% glycerol electrolyte containing 20mM bismuth nitrate pentahydrate ($Bi(NO_3)_3 \cdot 5H_2O$), 1.15M potassium nitrate ($KNO_3$), 0.33M L-tartaric acid ($2R,3R$-$(CHOHCOOH)_2$), and nitric acid ($HNO_3$). Firstly, supporting electrolyte was prepared by adding glycerol, potassium nitrate and tartaric acid to deionized water and stirring after full dissolution of the precursors. Then, bismuth nitrate was added to the electrolyte and, after that, nitric acid slowly dropped until the bismuth nitrate was completely dissolved (to pH~0.65±0.15). It is mandatory to mix the chemical products in this order to avoid the formation of insoluble bismuth compounds in the electrolyte.

### Electrodeposition

ECD was carried out by potential control at room temperature without electrolyte agitation, in a vertical three-electrode configuration with an Ag/AgCl (3M NaCl) acting as reference electrode. A platinum mesh was used as counter electrode, placed parallel to the surface of the working electrode. The working electrodes used in this work were PCMs supplied by Sterlitech, which present a template of parallel and cylindrical channels of 6μm length, from one side to the other of the PCM. The density of pores is $4\text{-}6\times10^8$ cm$^{-2}$ and the nominal tolerance of the pore diameter is +0% -20%. In this work, we report electroplating experiments using PCM of 10nm, 30nm, 50nm and 100nm in diameter. To use these membranes as a cathode, we firstly sputtered a thin polycrystalline Au layer at the bottom as a metallic contact at pressure of 10$^{-2}$ mbar.

### Preparation of the nanowires

After growth, the PCMs were rinsed with deionized water and dried by nitrogen. This process prevents deposits of bismuth compounds due to the evaporation of electrolyte remains. In this paper, we present measurements carried out by different techniques. It involves different ways to prepare the NWs. Some of them need the nanowires separated from the membrane whereas others techniques enable to preserve it. In both cases, we have removed the Au layer, leaning it against a mercury drop during 60s and rinsed later with abundant deionized water to eliminate possible Hg and/or Au residues. When released NWs were required, we inserted the PCM into 2ml of dichloromethane ($CH_2Cl_2$) and stirred softly (without soundsonic applied) for 5 minutes. Once we had the NWs in a dichloromethane solution, we could deposit a drop on the substrates or holders of the different techniques reported here. We want to remark that we have not found waste coming from the PCM or the Hg drop by the techniques carried out.

## Structural characterization

To characterize the morphology and microstructure of the bismuth nanowires, we carried out several experiments by *Scanning Electron Microscopy* (SEM). We performed a *High Resolution Transmission Electron Microscopy* (HRTEM) -equipped with Energy Dispersive X-ray Spectroscopy analysis (EDX) for composition analysis- and *Select Area Electron Diffraction* (SAED) to characterize the crystalline structure of the NWs individually. In order to obtain information about the crystalline structure of all deposited NWs in one membrane, we carried out *X-ray Diffraction* (XRD) with a Cu-K$_\alpha$ source ($\lambda$=1.54Å). In this particular case, we placed 5 pieces of PCM with NWs onto an amorphous glass holder and drop directly the dichloromethane to dissolve the membrane. We subtracted the amorphous contribution of the holder form the XRD measurements and later we normalized them to the most intense Bi reflection.

## Synchrotron radiation experiments

*X-ray Absorption Near Edge Structure* (XANES) spectra were measured in transmission configuration at the Bi L$_3$ edge (13424eV) at room temperature. We held several pieces of the PCM containing NWs with kapton tape to have a nominal thickness between 30 to 80 µm in the experiments. We performed measurements at five different places of each sample and calculated the averaged of them using *Athena Software* [34]. The incident and transmitted beams were monitored with an ion chambers. The first was filled with a mixture of N$_2$ and Ar mixture (4:1) whereas the latter was filled with Kr. The experiments were carried out in the Spanish CRG beamline (SpLine, BM25) of the European synchrotron radiation facility (ESRF).

## Electrical characterization

Four-probe electrical measurements have been carried out on individual NWs in a commercial Physical Properties Measurement System (PPMS) from Quantum Design in the temperature range from 300 K down to 5 K with a low-frequency current of 100 nA. Focused-ion-beam induced-deposition (FIBID) was used to grow four tungsten nanocontacts on each individual NW, connecting them to Al contact pads placed on the sample holder.

## Acknowledgements

## References

[1] Manguez, J.H;  Issi, J.P., Heremans , J. Transport properties of bismuth in quantizing magnetic fields. Phys. Rev. B. **1976**, 14, 4381-4385

[2] N. García, N; Strongin, M; Kao, Y.H. Phys. Rev. B. **1972**, 5, 2029-2039

[3] Liu, K.; Chien, C.L.; Searson, P.C. Finite-size effects in bismuth nanowires. Phys. Rev. B. **1998**, 58, R14681-R14684

[4] Yang, F.Y.; Strijkers, G.J.; Hong, K.; Reich, D.H.; Searson, P.C.; Chien, C.L.; Large magnetoresistance and finite-size effects in electrodeposited bismuth lines. J. Appl. Phys. **2001**, 89, 7206-7208

[5] Farhangfar, S. Quantum size effects in a one-dimensional semimetal. Phys. Rev B. **2006**, 74, 205318

[6] Farhangfar, S. Quantum size effects in solitary wires of bismuth. Phys. Rev. B. **2007**, 76, 205437

[7] Cornelius, T.W.; Toimil-Molares, M.E.; Karim, S; Neumann, R. Oscillations of electrical conductivity in single bismuth nanowires. Phys. Rev. B. **2008**, 77, 125425

[9] Huber,T.E.; Nikolaeva, A; Gitsu, D.; Konopko, L; Foss Jr., C.A.; Graf, M.J.; Confinement effects and surface-induced charge carries in Bi quantum wires. Appl. Phys. Lett. **2004**, 84, 1326-1328

[9] Huber,T.E.; Nikolaeva, A; Konopko, L; Graf, M.J. Observation of three-dimensional behavior in surface states of bismuth nanowires and the evidence for bulk-Bi surface quasiparticles. Phys. Rev. B. **2009**, 79, 201304(R)

[10] Marcano, N; Sangiao, S; Plaza, M; Perez, L; Fernández-Pacheco, A; Córdoba, R; Sánchez, M.C.; Morellón, L; Ibarra, M.R; De Teresa, J.M. Weak-Antilocalization signatures in the magnetotransport properties of individual electrodeposited Bi Nanowires. Appl. Phys. Lett. **2010**, 96, 08210X

[11] Ye, Z.; Zhang, H.; Liu, H.; Wu, W.; Luo, Z.; Evidence for superconductivity in single crystalline Bi nanowires. Physica B **2008**, 403, 1529-1530

[12] Nikolaeva, A; Huber, T.E.; Gitsu, D.; Konopko, L.; Diameter dependent thermopower of bismuth nanowires, Phys. Rev. B **2008**, 77, 035422

[13] Tahboub, R.M.; El Guindy, M.; Merchant, H.D. Oxidation kinetics of bismuth and its dilute alloys. Oxidation of metals. **1979**, 13, 545-556.

[14] Sharma, S.K.; Pandey, S.L. Structure of thermally oxidized bismuth films. Thin Solid Films, **1979,** 62, 209-214.

[15] Cronin, S.B.; Lin, Y.-M.; Rabin, O.; Black, M.R.; Ying, J.Y.; Dresselhaus, M.S.; Gai, P. L.; Minet, J-P.; Issi, J-P.; Making electrical contact to nanowires with a thick oxide coating. Nanotechnology **2002**, 13, 653-658

[16] Bisrat, Y.; Luo, Z.P.; Davis, D.; Lagoudas, D. Higly ordered uniform single-crystal Bi nanowires: fabrication and characterization. Nanotechnology **2006**, 18, 395601

[17] Shim, W.; Ham, J.; Lee, K.; Jeung, W.Y.; Johnson, M.; Lee, W. On-film formation of Bi nanowires with extraordinary electron mobility. Nanoletters **2009** 9, 18-22

[18] Liu, K; Chien, C.L.; Searson, P.C.; Yu-Zhang, K. Structural and magneto-transport properties of electrodeposited bismuth nanowires. Appl. Phys. Lett. **1998,** 73, 1436

[19] Cornelius, T.W.; Brötz, J; Chtanko, N; Dobrev, D; Miehe, G; Neumann, R; Toimil Molares, M.E.; Controlled fabrication of poly- and single-crystalline bismuth nanowires, Nanotechnology, **2005**, 16, S246–S249

[20] Tian, Y.T.;  Meng, G. M.; Wang, G. Z.; Phillipp, F.; Sun S.H.; Zhang, L.D. Step-shaped bismuth nanowires with metal–semiconductor junction characteristics. Nanotechnology, **2006**, 17, 1041-1045.

[21] C.A. Jeffrey, D.A. Harrington and S. Morin, In situ scanning tunneling microscopy of bismuth electrodeposition on Au(111) surfaces. Surface Science 2002, 512, (1-2), L367-L372

[22] E. Sandnes, M.E. Williams, U. Bertocci, M.D. Vaudin and G.R. Stafford, Electrodeposition of bismuth from nitric acid electrolyte. Electrochimica Acta  2007, 52, (21), 6221-6228.

[23] Chen, C. H.; Kepler, K. D.; Gewirth, A. A.; Ocko, B. M.; Wang, J., Electrodeposited Bismuth Monolayers On Au(111) Electrodes - Comparison Of Surface X-Ray-Scattering, Scanning-Tunneling-Microscopy, And Atomic-Force Microscopy Lattice Structures. J. Phys. Chem. 1993, 97, (28), 7290-7294.

[24] B. K. Niece and A.A. Gewirth, Potential-step chronocoulometric investigation of the surface coverages of coadsorbed Bi and hydroxide on Au(111) electrodes. Langmuir 1996, 12, (20), 4909-4913.

[25] K. Tamura, J.X. Wang, R.R. Adzic and B.M. Ocko, Kinetics of monolayer Bi electrodeposition on Au(111): Surface X-ray scattering and current transients. Journal of Physical Chemistry B 2004, 108, (6), 1992-1998

[26] Whitney, T.M.; 1, Searson, P.C.; Jiang, J.S.; Chien, C.L.; Fabrication and Magnetic Properties of Arrays of Metallic Nanowires. Science, **1993**, 3, 5126, 1316 -1319.

[27] O´Brien, B.; Plaza, M.; Zhu, L.Y.; Pérez, L.; Chien, C.L., Searson, P.C.; Magnetotransport Properties of Electrodeposited Bismuth Films. J. Phys. Chem. C, **2008**, 112, 12018–12023

[28] Hyde, M.E.; Compton, R.G.; A review of the analysis of multiple nucleation with diffusion controlled growth J. Electroanal. Chem. **2003,** 549, 1.

[29] http://www.sterlitech.com/37625/Polycarbonate-Membranes-PCTE.html

[30] http://www.panalytical.com/index.cfm?pid=546

[31]  Retoux, R.; Studer, F.; Michel, C.; Raveau, B.; Fontaine, A.; Dartyge, E. Valence state for bismuth in the superconducting bismuth cuprates. Phys. Rev. B. **1990,** 41, 193-199.

[32] Witkowska, A.; Rybicki, J.; Di Cicco, A. EXAFS analysis of bismuth atom neighborhood in reduced bismuth silicate glass. Phys. Chem. Glasses, 2002, 43C, 124–7.

 [34] http://cars9.uchicago.edu/~ravel/software/

Figure captions


**Figure 1.** (a) Time dependence of the current for 20mM of Bi(III) at -75mV in PCM of 100nm of pore size. Dashed lines divide the curve in 3 different regimes: (i) nucleation, (ii) constant growth and (iii) saturation. (b) TEM image of Bi NW presenting the Au seed. More details in the text. Figures (c) and (d) present SEM images for Bi NWs grown in PCMs of pore diameter of 10nm and 30nm respectively.


**Figure 2.** (a) XRD patterns for Bi NWs deposited varying the porous diameter. Figures (b) and (c) are HRTEM images of the edge of a Bi NW. Red arrows point to [012] direction whereas the yellow ones point to growth direction. i and ii denote low dimensional defects. (d) SAED pattern identifying the family of planes [110], [003] and [113]. (e) HRTEM image of 80nm diameter Bi NW which denotes the presence of an amorphous shell.


**Figure 3.** (a) XANES spectrum of Bi, BiO and oxidized and unoxidized NWs of several diameters (solid lines). Dotted lines denote the calculated spectrum following the equation 1. Values of p are shown in the text. (b) Derivative spectrum of the curves showed in figure 3.a. A1, A2 and A3 denote the characteristic peaks for Bi whereas B is characteristic for BiO. (c) Detail of the XRD pattern for Bi NWs after 10 days in presence of atmospheric oxygen. Solid line indicates the position of Bi[012]. Dashed line represents the position of the new peak due to the oxidation process.

**Figure 4.** (a) Temperature-dependent resistance for the 100 nm-diameter Bi nanowire. (b) A SEM image showing and individual 100-nm-diameter Bi nanowire with four Focused-ion-beam-induced-deposited Tungsten nanoelectrodes (FIBID-W). (c) Four-point I-V curves taken at both 5 K and room temperature for the Bi nanowire device.
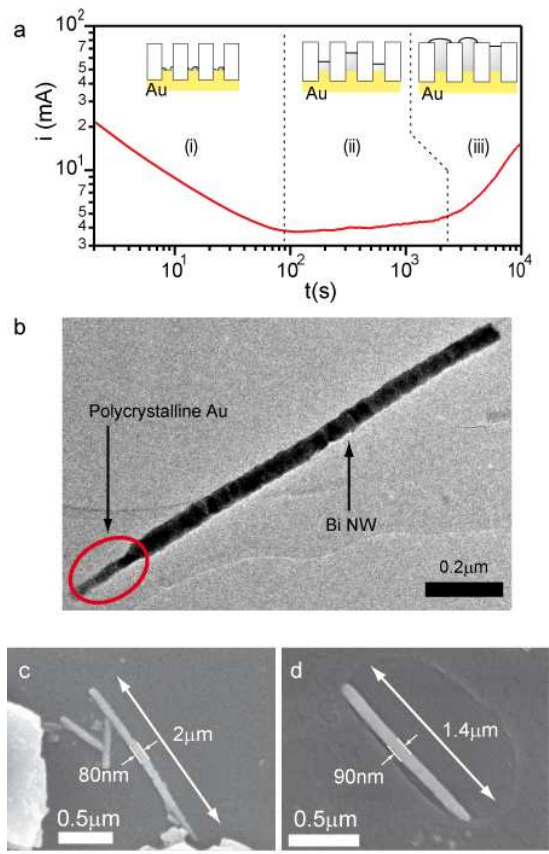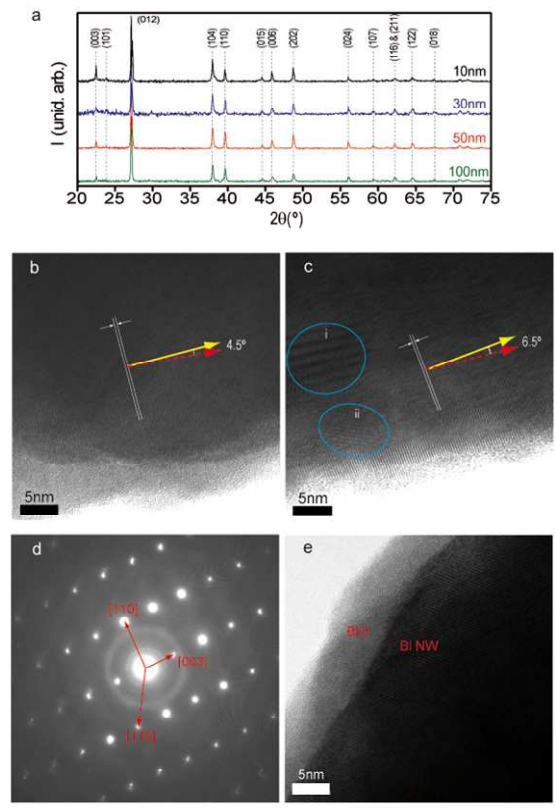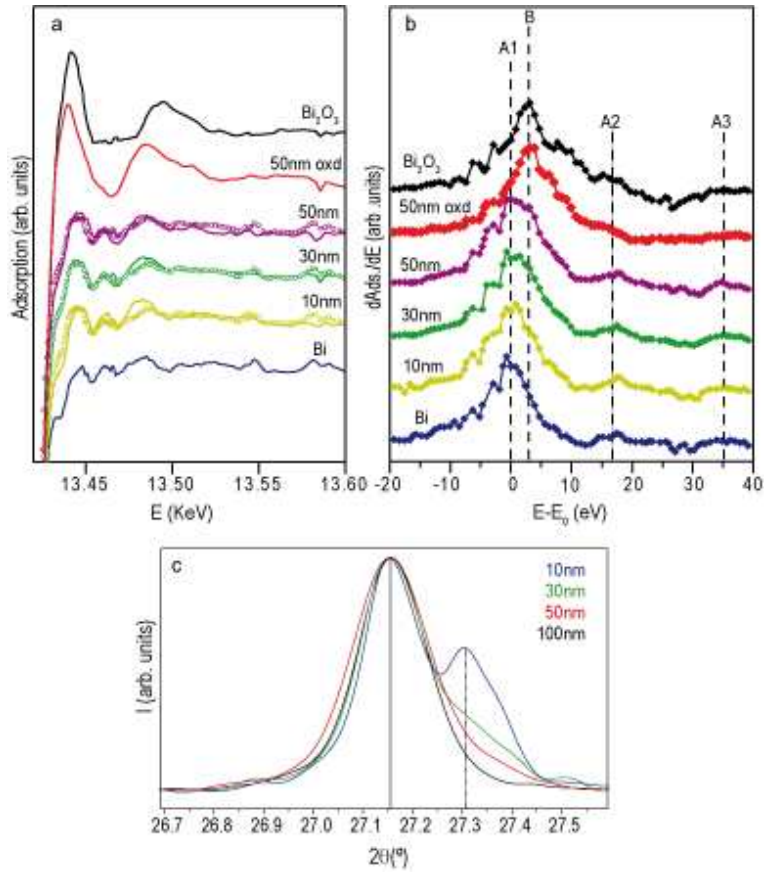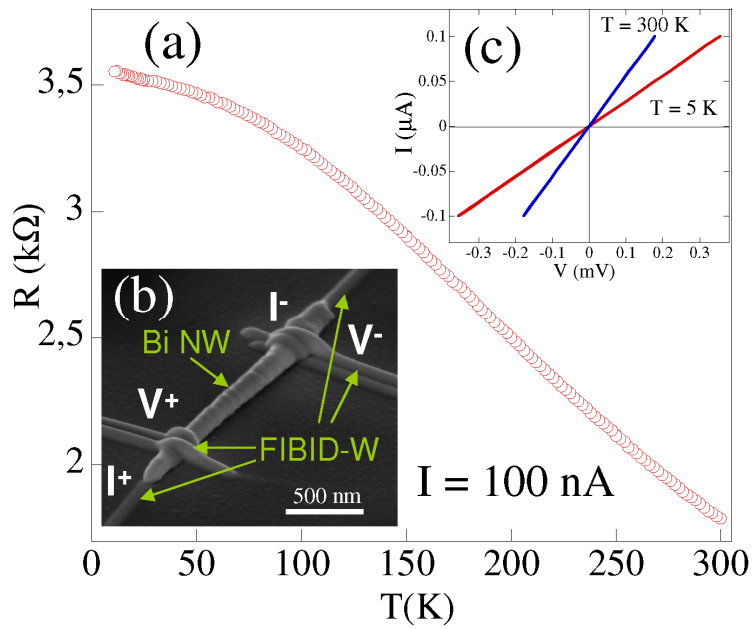
Figure 1.



Figure 2.

Figure 3.



Figure 4.